

## Corrosion of titanium alloys in pressurized water at 300 °C and 15 MPa

Quentin BIGNON<sup>1,2</sup>, Quentin AUZOUX<sup>1\*</sup>, Frantz MARTIN<sup>1</sup>, Amandine RAYNAL<sup>1</sup>, Frédéric MISERQUE<sup>1</sup>, Michel TABARANT<sup>3</sup>, Laurence LATU-ROMAIN<sup>2</sup>, Yves WOUTERS<sup>2</sup>

<sup>1</sup>Den-Service de la Corrosion et du Comportement des Matériaux dans leur Environnement (SCCME), CEA, Université Paris-Saclay, F-91191, Gif-sur-Yvette, France

<sup>2</sup>Université Grenoble Alpes, CNRS, SIMaP, F-38402 Saint Martin d'Hères, France

<sup>3</sup>Den-Service d'Etudes Analytiques et de Réactivité des Surfaces (SEARS), CEA, Université Paris-Saclay, F-91191, Gif-sur-Yvette, France

\*corresponding author, [quentin.auzoux@cea.fr](mailto:quentin.auzoux@cea.fr), DEN/DANS/DPC/SCCME/LECA, Bâtiment 458, Point Courrier 50, CEA Saclay, 91191 Gif-sur-Yvette, France

### Abstract

Commercially pure titanium (Ti CP) and two titanium alloys (Ti 64 and Ti10-2-3) representative of different metallurgical classes were exposed to pressurized water at 300 °C, 15 MPa in a dedicated stainless steel corrosion loop up to 1632 h.

Mass uptake measurements as well as extensive characterization of the oxides formed on the polished samples using scanning and transmission electron microscopy, Raman spectroscopy, X-ray diffraction, X-ray photoelectron spectroscopy, photoelectrochemistry and glow discharge optical emission spectroscopy led to the following main conclusions:

- The oxide scale was made of a thin and continuous TiO<sub>2</sub> layer topped by small TiO<sub>2</sub> anatase crystallites and large FeTiO<sub>3</sub> ilmenite crystallites.
- The interface tortuosity increased with exposure duration, as well as the amount of crystallites. From 217 h exposure, the thickness of the thin continuous TiO<sub>2</sub> layer remained constant with exposure duration.
- The mass uptake increased approximatively linearly with exposure duration.

These observations were consistent with a corrosion mechanism involving simultaneous oxide growth, dissolution and precipitation. The corrosion rate of the three studied materials was estimated to be around 3 µm/year.

### Introduction

Titanium alloys could be good candidates for nuclear Pressurized Water Reactor (PWR) primary circuit structure components because of their low neutron activation and their good mechanical properties. However, their corrosion resistance in such conditions (15 MPa, 300 °C) is poorly known.

A few studies investigated the corrosion behaviour of titanium alloys in liquid water environment at such temperature [1–6]. For example, Kaneda et al. [1] studied the corrosion resistance of different α/β and β titanium alloys exposed 500 h to supercritical water (25 MPa, 290–550 °C). Thin oxide films (less than 1 µm) covered by dispersed particles were observed at 290 °C for both α/β and β alloys but the composition of the oxides was not investigated at this temperature. Corrosion mechanisms and corrosion rate of titanium alloys in pressurized water at 300 °C are therefore still undetermined.

The present study aims at quantifying the corrosion resistance of commercially pure titanium and of two titanium alloys representative of different metallurgical classes in pressurized water at 300 °C and 15 MPa. Flat polished specimens were first exposed to this environment in a dedicated corrosion loop. The oxides formed were then characterized using complementary techniques. Finally, a corrosion mechanism consistent with all the obtained results was proposed and the corrosion rate was estimated.

### Materials and experiments

#### Materials

Commercially pure titanium (Ti CP) and two titanium alloys (Ti 64 and Ti10-2-3) were studied in their mill-annealed state. Ti CP is a single phase α commercially pure titanium (ASTM grade 2), Ti 64 or Ti6Al-4V (ASTM grade 5) is a two-phase α/β titanium alloy containing 4 vol% of β phase and Ti10-2-3 or Ti10V2Fe-3Al is a two-phase β metastable alloy containing 38 vol% of β phase. Their chemical composition was in accordance with the ASTM and AMS standards [7, 8]. More information about the microstructure and the crystallographic texture of the materials can be found in [9]. 1.2-mm thick rectangular specimens (1 cm × 2 cm) were cut from the billets, then ground with SiC paper and polished with diamond paste and finally with a colloidal silica suspension at pH = 9.

#### Exposure of the specimens to pressurized water

The polished specimens were exposed to pressurized water at 300 °C and 15 MPa in a stainless steel corrosion loop. Lithium hydroxide (3.1 mg<sub>LiOH</sub>/kg<sub>H<sub>2</sub>O</sub>) was added to the water to set the pH<sub>25 °C</sub> value at 10.1, which corresponded to a pH<sub>300 °C</sub> of 7.5 [10]. A dissolved hydrogen concentration of 2.25 mg<sub>H<sub>2</sub></sub>/kg<sub>H<sub>2</sub>O</sub> was imposed by the hydrogen gas pressure (0.14 MPa) in the vessel of the cold part of the loop. The water flow was 5 × 10<sup>-3</sup> m<sup>3</sup>.h<sup>-1</sup> leading to a water speed inside the reactor of 7.2 m.h<sup>-1</sup> during tests. After having been cooled down the whole water volume went through an ion-exchange resin tank in order to capture a part of the corrosion products dissolved in the water. The ion exchange resin was saturated with lithium hydroxide before the test campaign in order to avoid any variation of lithium concentration during tests. New samples were used for every studied exposure duration.

#### Post-exposure characterization techniques

The nature and morphology of the oxide scales formed on the specimens were determined by scanning and transmission electron microscopy (SEM and TEM), Raman spectroscopy, X-ray diffraction (XRD), X-ray photoelectron spectroscopy (XPS) and photoelectrochemistry. The evolution of the samples with increasing exposure duration was quantified by SEM image analysis of cross sections, glow discharge optical emission spectroscopy (GD-OES) and mass uptake. In order to prevent oxide degradation during preparation of the cross sections for observation by SEM, the specimens were previously electrochemically plated with nickel. Mass uptake measurements were done by weighing of each specimen before and after exposure on a Mettler Toledo XP205 scale. More details regarding the characterization techniques were reported in [9].

### Results

#### Nature and morphology of the oxides

Figure 1 shows a SEM image and energy dispersive spectroscopy (EDS) mapping of the surface of a Ti CP sample exposed during 434 h. Two types of crystallites were discriminated. The first one is constituted by relatively large crystallites (3–10 µm) containing titanium, iron and oxygen and the second one is constituted by relatively small crystallites (0.3–1 µm) containing only titanium and oxygen. These two types of crystallites were observed on the three studied materials after all exposure durations. Local Raman spectroscopy presented in [9] allowed the identification of the crystallographic phase of these two types of crystallites: FeTiO<sub>3</sub> ilmenite for the larger crystallites and TiO<sub>2</sub> anatase for the smaller ones.

The X-ray diffractograms showed in Figure 2 confirmed the presence of these two oxide phases along with the metallic titanium phases: a for all materials and b for Ti 64 and Ti10-2-3. Noticeable was also the presence of TiO<sub>2</sub> rutile on Ti CP sample exclusively.

Complementary analysis by ASTAR-TEM presented in Figure 3 enabled to identify this phase as a thin continuous oxide layer located on Ti CP at the interface between the metal and the environment. ASTAR-TEM analysis also confirmed the absence of TiO<sub>2</sub> rutile on Ti 64 and Ti10-2-3 alloys. The thin continuous oxide layer that was observed by TEM and SEM on these alloys was made of TiO<sub>2</sub> anatase, so that the frontier between small crystallites and the continuous layer did not appear as clearly as on Ti CP.

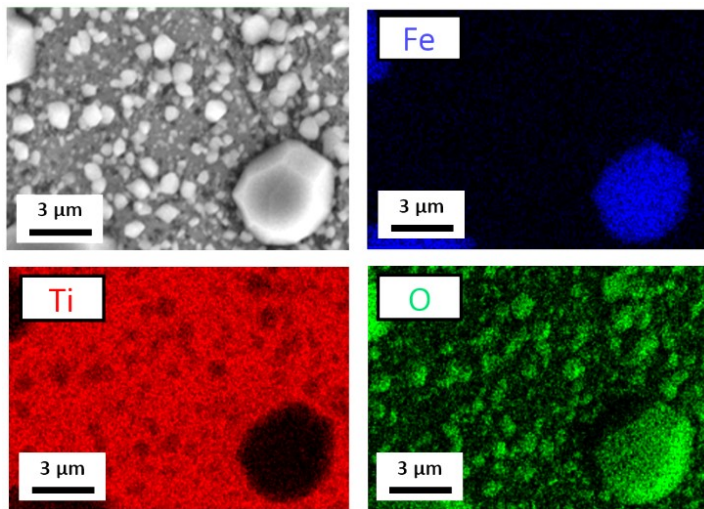


Figure 1: SEM secondary electrons image (top left) and EDS mapping (E = 20 kV) of Ti CP sample surface exposed during 434 h to pressurized water at 300 °C and 15 MPa [9]

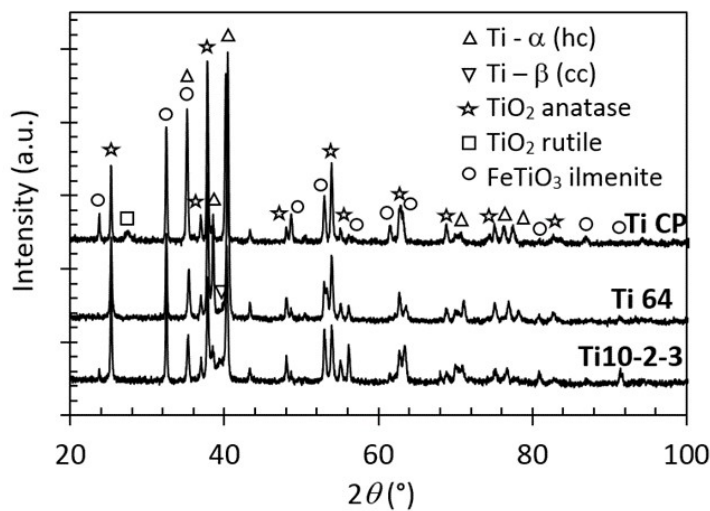


Figure 2: Diffractograms of Ti CP, Ti 64 and Ti10-2-3 samples exposed during 434 h to pressurized water at 300 °C and 15 MPa [9]

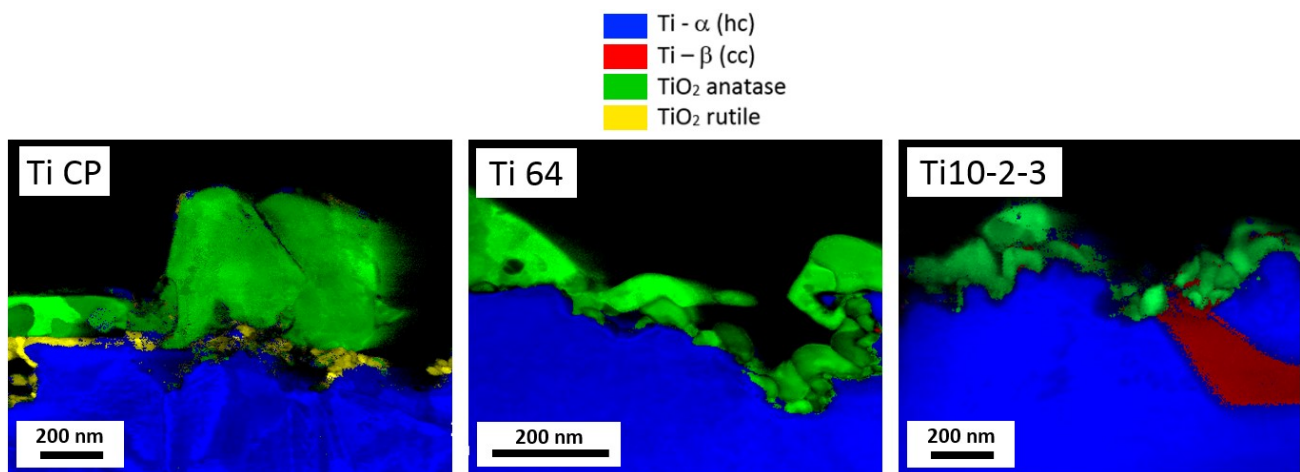


Figure 3: ASTAR-TEM phase maps of oxide scales on Ti CP, Ti 64 and Ti10-2-3 samples exposed during 434 h to pressurized water at 300 °C and 15 MPa [9]

*Evolution of the samples with increasing exposure durations*

Figure 4 shows SEM images of the cross sections of Ti CP samples exposed respectively 217 h, 434 h and 834 h to pressurized water at 300 °C and 15 MPa. The cross sections of the other studied materials (not shown here) presented the same features. The continuous oxide layer thickness was found to remain constant from 217 h up to 1632 h. The mean thickness values

measured by SEM were approximately 30, 24 and 22 nm for Ti CP, Ti 64 and Ti10-2-3, respectively. As the exposure duration increased, the tortuosity of the interface between the materials and the environment increased. The mean corroded metal depth was defined as the quotient of the volume of corroded metal by the initial surface of the sample. It was estimated following the method illustrated in Figure 5. For each exposure duration and each studied material, 20 SEM images were analysed. Figure 6a shows that the mean corroded metal depth increased as function of the exposure duration in an approximate linear way. Figure 6b indicates that the ratio of the maximum corrosion penetration depth to the mean corroded metal depth was near 3.5:1 for all studied materials and all exposure durations.

GD-OES was used to quantify the ratio of the amount of FeTiO<sub>3</sub> ilmenite to the total quantity of oxide (both FeTiO<sub>3</sub> and TiO<sub>2</sub>). Figure 7 indicates that this ratio (referred to as *q* in the following section) never exceeded 0.22. The main oxide formed on the samples was therefore TiO<sub>2</sub>. Figure 7 also indicates that this ratio was lower for Ti 64 than for the two other studied materials and that it increased with the exposure duration.

Mass uptake values as function of exposure duration are presented in Figure 8. They increased almost linearly with exposure duration. Mass uptake of Ti 64 was slightly lower than Ti CP and Ti10-2-3 ones.

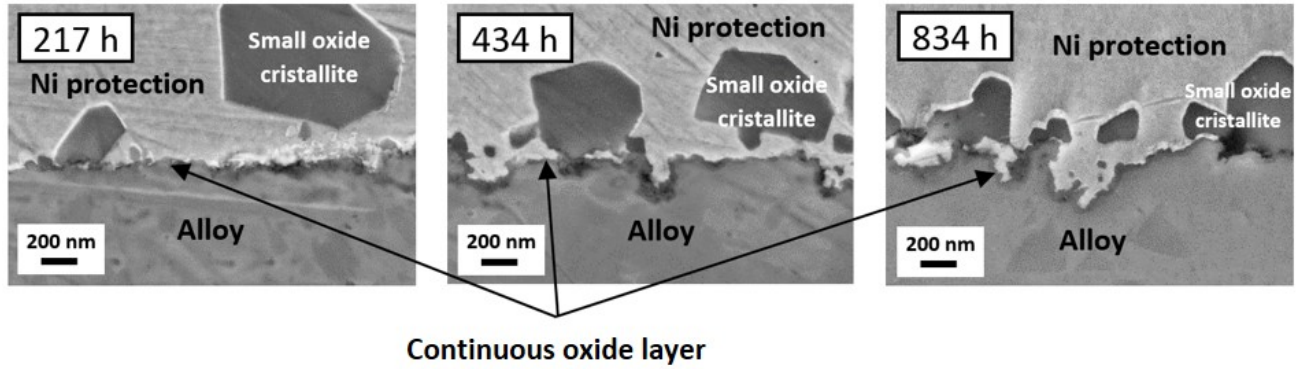


Figure 4: SEM observation (secondary electrons) of cross sections of Ti CP samples exposed respectively 217 h, 434 h and 834 h to pressurized water at 300 °C and 15 MPa [9]

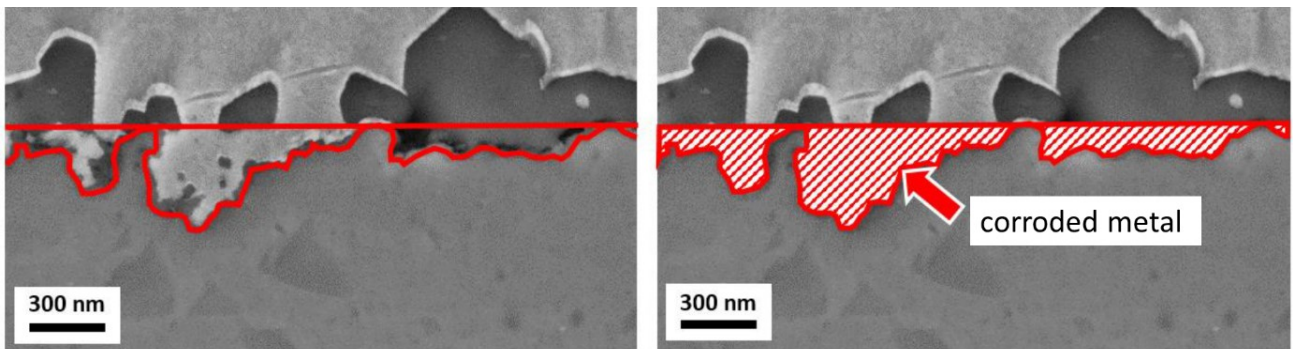


Figure 5: Illustration of the image analysis method used to estimate of the mean corroded metal depth (quotient of the hatched area by the width of the image) from SEM observations of cross sections of exposed samples

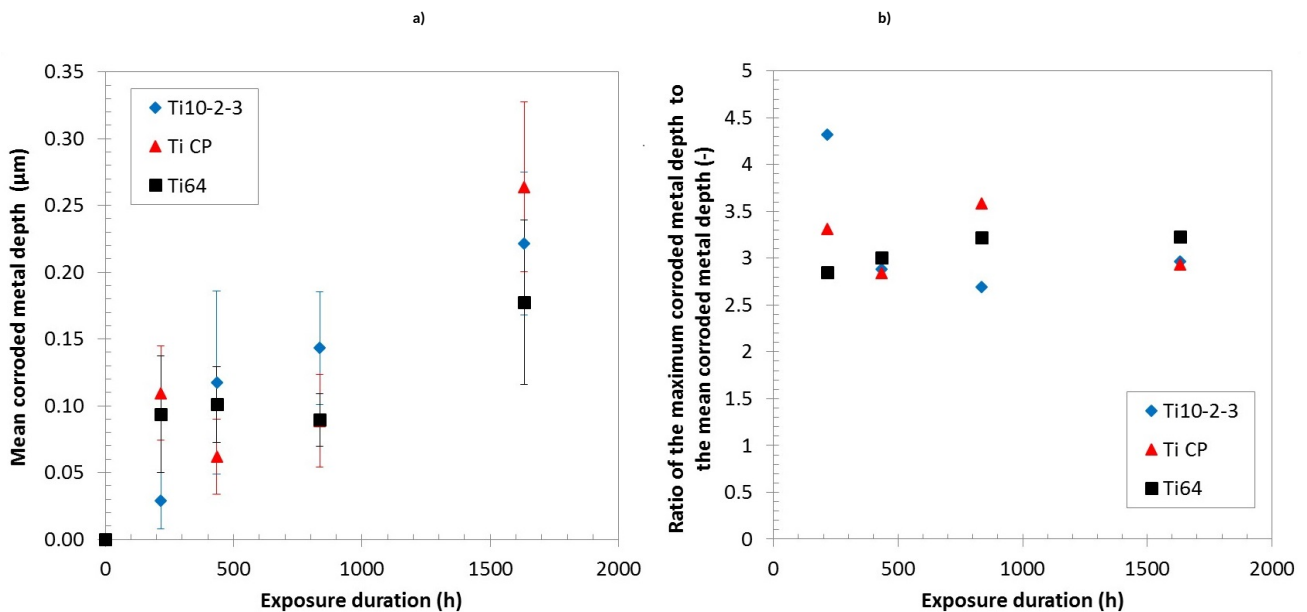


Figure 6: Mean corroded metal depth (a) and maximum to mean corroded metal depth ratio (b) estimated from SEM observations of cross sections of samples exposed to pressurized water at 300 °C and 15 MPa

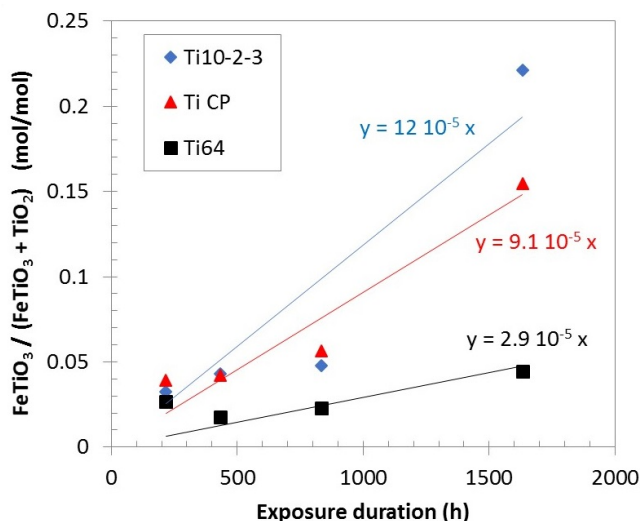


Figure 7: Ratio (referred to as q) of the amount of FeTiO<sub>3</sub> ilmenite to the total amount of oxide (both FeTiO<sub>3</sub> and TiO<sub>2</sub>) determined by GD-OES after exposure of the samples to pressurized water at 300 °C and 15 MPa

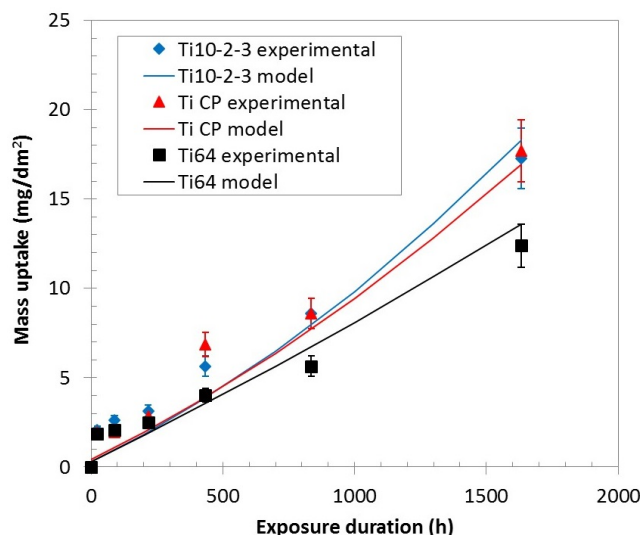


Figure 8: Mass uptake measured after exposure of the samples to pressurized water at 300 °C and 15 MPa (experimental) and following the model described in the discussion section (Eq.1 with  $p = 0.9$ ,  $r = 2.8$   $\mu\text{m}/\text{year}$  and  $q$  according to equations of Figure 7)

## Discussion

### Corrosion mechanism

The increase of interface's tortuosity with exposure duration along with the steadiness of the continuous oxide layer's thickness indicate that this TiO<sub>2</sub> layer underwent simultaneous dissolution and growth. This type of mixed corrosion mechanism was modelled by Haycock [11]. In the present case, the continuous oxide layer growth was assumed to be controlled by the diffusion of oxygen vacancies through the layer because it was found to grow inwards and to be a n-type semi-conductor [9]. The growth rate therefore decreased as the thickness increased during the first transitory period. During this period, the oxide layer growth is significantly faster than the dissolution, leading to an increase of the oxide thickness from ~4 nm (native continuous oxide thickness) up to ~25 nm (stationary continuous oxide thickness). At such thickness, growth rate and dissolution rate are equal so that the thickness remained constant.

Such a mechanism is consistent with the significant value of the TiO<sub>2</sub> solubility in water in the conditions of the study (around  $1.2 \times 10^{-8}$  mol. kg<sup>-1</sup> H<sub>2</sub>O [12]). Titanium species potentially formed by the dissolution of TiO<sub>2</sub> in water at pH = 7.5 and 300 °C are Ti(OH)<sub>4</sub> and Ti(OH)<sub>5</sub><sup>-</sup> hydroxides [13]. The presence of TiO<sub>2</sub> anatase crystallites on the continuous oxide layer surface of all studied material for all exposure durations indicates that dissolved titanium hydroxides have then reprecipitated. Part of these hydroxides co-precipitated with iron hydroxides (most probably originated from the corrosion of the stainless steel pressure vessel) forming FeTiO<sub>3</sub> ilmenite.

Noticeable is the fact that no aluminium nor vanadium was detected in the oxides formed on Ti 64 and Ti10-2-3. The present authors still believe that these elements were oxidized and incorporated as cations in the thin continuous TiO<sub>2</sub> oxide and finally dissolved in the water. Aluminium oxides solubility is indeed very high at 300 °C and pH = 7.5 (around 10<sup>-3</sup> mol.kg<sup>-1</sup> H<sub>2</sub>O [14]). As the contribution of the continuous oxide layer to the overall oxide formed on the samples was very low, potential presence of aluminium and vanadium in this layer was not detectable by GD-OES nor XPS.

Characterization by ASTAR-TEM, SEM and XRD revealed that the continuous TiO<sub>2</sub> layer was made of rutile on Ti CP sample and made of anatase on Ti 64 and Ti10-2-3 samples. This result is consistent with the bandgap values measured by photoelectrochemistry presented in [9]. The TiO<sub>2</sub> crystallites were made of anatase on all materials. Rutile is for all temperature and pressure conditions the thermodynamic stable phase of TiO<sub>2</sub>. However, due to kinetics, low temperatures such as 300 °C favor anatase formation, which is consistent with the anatase crystallites observation. Impurities and dopants favor the formation of either rutile (like hydrogen, lithium and vanadium) or anatase (like aluminium) [15-17]. In the present case, we believe that a part of the hydrogen produced by the reduction of water balancing titanium oxidation is incorporated in the continuous oxide layer. When the material does not contain aluminium, this hydrogen doping appears to have the dominant effect (leading to rutile formation on Ti CP); otherwise, the effect of aluminium doping appears to dominate (leading to the formation of anatase on the other studied materials).

#### Corrosion rate

The quantification of the mean corroded metal depth as function of exposure duration based on cross sections observation by SEM (Figure 6a) led to the following estimation of the corrosion rate: -1.2 µm/year for the three studied materials. As the reference line used in this method might not correspond to the real initial surface position, this estimation is obviously a lower bound. Figure 6b indicates that the corrosion rate could reach locally a 4 times higher value. Nevertheless, as the ratio of the maximum corrosion penetration depth to the mean corroded metal depth remained constant while exposure duration increased (Figure 6b), the corrosion appeared relatively homogeneous. In particular, no preferential corrosion of alpha phase or beta phase was observed for Ti 64 or Ti10-2-3.

Following the mechanism proposed in the previous section, mass uptake per unit area  $Dm/S$  (g.cm<sup>-2</sup>) results from three contributions. The first one is the mass gain due to oxygen involved in the growth of the continuous oxide layer; the second one is the mass gain due to oxygen and iron precipitated on the surface in either TiO<sub>2</sub> anatase or FeTiO<sub>3</sub> ilmenite crystallites; the last one is the potential mass loss due to the titanium (and alloying elements) that was dissolved in the water and that did not precipitate as crystallites on the sample.

Eq. 1 is an approximation of this mass uptake, where  $De$  represents the increase in the continuous oxide layer thickness (cm),  $M_i$  and  $r_i$  the molar mass (g.mol<sup>-1</sup>) and the density (g.cm<sup>-3</sup>) of the  $i$  specie,  $r$  the corrosion rate (cm.s<sup>-1</sup>),  $t$  the time (s) from the beginning of the exposure,  $p$  the ratio of precipitated titanium to dissolved titanium and  $q$  the ratio of the amount of FeTiO<sub>3</sub> to the total amount of oxides. In the present experimental conditions, the first term was much lower than the second one. In other words, the mass uptake resulted almost exclusively from the micrometric crystallites rather than from the nanometric continuous layer. This equation also emphasizes the fact that, with such a mixed oxide dissolution and precipitation corrosion mechanism, mass uptake could be negative for  $p$  values inferior to 0.6. In the present case, the mass uptake experimental values were positive (Figure 8). They were used along with the  $q$  ratio estimated by GD-OES (Figure 7), to estimate the corrosion rate according to Eq. 1. Values of 2.2, 2.8 and 3.8 µm/year were found for  $p$  values of 1, 0.9 and 0.8, respectively, which is consistent with the lower bound determined previously.

As illustrated in Figure 8, this model suggests that the lower mass uptake of Ti 64 in comparison to the other studied materials originated from a lower ilmenite precipitation (lower  $q$  ratio) rather than from a lower corrosion rate.

$$\frac{\Delta m}{S} = \Delta e \frac{\rho_{TiO_2}}{M_{TiO_2}} M_{O_2} + r t \frac{\rho_{Ti}}{M_{Ti}} [p(M_{O_2} + qM_{FeO}) - (1-p)M_{Ti}] = \Delta e \frac{\rho_{TiO_2}}{M_{TiO_2}} M_{O_2} + r t \rho_{Ti} \left[ p \frac{M_{TiO_2} + qM_{FeO}}{M_{Ti}} - 1 \right] \quad \text{Eq.1}$$

## Conclusion

In pressurized water at 300 °C, 15 MPa and pH<sub>300 °C</sub> = 7.5, the corrosion rate of commercially pure titanium and of two titanium alloys representative of different metallurgical classes was found to be around 3 µm/year.

The corrosion rate appeared to be controlled by the dissolution of the continuous nanometric TiO<sub>2</sub> oxide layer that formed on the surface of the studied materials. Growth of this oxide layer occurred at the metal-oxide interface and was assumed to be controlled by the diffusion of oxygen vacancies.

In the present experimental conditions, the major part of the dissolved TiO<sub>2</sub> continuous oxide re-precipitated on the specimens as both TiO<sub>2</sub> anatase and FeTiO<sub>3</sub> ilmenite crystallites. Iron involved in ilmenite precipitation was believed to originate from the corrosion of the pressure vessel made of stainless steel.

## Acknowledgements

This research was funded by CEA. The studied materials were provided by TIMET. The authors warmly thank Frédéric Datcharry from CEA Saclay for the design and fabrication of the corrosion loop.

## References

1. J. Kaneda, S. Kasahara, J. Kuniya, K. Moriya, F. Kano, N. Saito, A. Shioiri, T. Shibayama, H. Takahashi, Proceedings of the 12th International Conference on Environmental Degradation of Materials in Nuclear Power System Water Reactors, The Minerals, Metals & Materials Society (2005) 1409–1418.
2. J.-S. Lu, Z.-Y. Mao, J.-Y. Zhang, C.-A. Ma, X.-B. Mao, X.-H. Li, Trans. Nonferrous Met. Soc. China 12 (2002) 1054–1057.
3. X. Tang, S. Wang, L. Qian, Y. Li, Z. Lin, D. Xu, Y. Zhang, Chem. Eng. Res. Des. 100 (2015) 530–541.
4. S.Y. Park, Proceedings of the Korean Nuclear Society Autumn Meeting (2004) 915–916.
5. B.S. Choi, Design Features of SMART Water Chemistry, Pittsburgh USA (2004) 39–45.
6. I.V. Gorynin, Mater. Sci. Eng. A 263 (2) (1999) 112–116.
7. ASTM B265-15 (2015) West Conshohocken, PA.
8. AMS4983A (1994) SAE International.
9. Q. Bignon, F. Martin, Q. Auzoux, F. Míserque, M. Tabarant, L. Latu-Romain, Y. Wouters, Corr. Sci., 150 (2019) 32–41.
10. A. V. Bandura and S. N. Lvov, J. Phys. Chem. Ref. Data, 35 (1) (2006) 15–30.
11. E. W. Haycock, J. Electrochem. Soc., 106 (9) (1959) 764–771.
12. K.G. Knauss, M.J. Dibley, W.L. Bourcier, H.F. Shaw, Appl. Geochem. 16 (9) (2001) 1115–1128.
13. W.G. Cook, R.P. Olive, Corr. Sci. 58 (2012) 291–298.
14. P. Bénézeth, D. A. Palmer, et D. J. Wesolowski, Geochim. Cosmochim. Acta, 65 (13) (2001) 2097–2111.
15. R.D. Shannon, J. Appl. Phys. 35 (11) (1964) 3414–3416.
16. N. Khatun, Anita, P. Rajput, D. Bhattacharya, S.N. Jha, S. Biring, S. Sen., Ceram. Int. 43(16) (2017) 14128–14134.
17. G.C. Vásquez, M.A. Peche-Herrero, D. Maestre, A. Gianoncelli, J. Ramírez-Castellanos, A. Cremades, J.M. González-Calbet, J. Piqueras, J. Mater. Chem. C 2 (48) (2014) 10377–10385.